Monthly Notices of the ROYAL ASTRONOMICAL SOCIETY

MNRAS **525,** 3330–3343 (2023) https://doi.org/10.1093/mnras/stad2367
Advance Access publication 2023 August 03

Digging a little deeper: characterizing three new extreme ULX candidates

T. P. Roberts [1]★ D. J. Walton [2] A. D. A. Mackenzie,[1] M. Heida[3] and S. Scaringi [1]

[1]*Centre for Extragalactic Astronomy & Dept of Physics, Durham University, South Road, Durham DH1 3LE, UK*
[2]*Centre for Astrophysics Research, University of Hertfordshire, College Lane, Hatfield AL10 9AB, UK*
[3]*European Southern Observatory, Karl-Schwarzschild-Str 2, D-85748 Garching bei München, Germany*

Accepted 2023 July 31. Received 2023 July 31; in original form 2023 June 2

ABSTRACT

A prime motivation for compiling catalogues of any celestial X-ray source is to increase our numbers of rare subclasses. In this work, we take a recent multimission catalogue of ultraluminous X-ray sources (ULXs) and look for hitherto poorly-studied ULX candidates that are luminous ($L_X \geq 10^{40}$ erg s^{-1}), bright ($f_X \geq 5 \times 10^{-13}$ erg cm^{-2} s^{-1}), and have archival *XMM–Newton* data. We speculate that this luminosity regime may be ideal for identifying new pulsating ULXs (PULXs), given that the majority of known PULXs reach similar high luminosities. We find three sources that match our criteria and study them using archival data. We find 4XMM J165251.5−591503 to possess a bright and variable Galactic optical/IR counterpart, and so conclude it is very likely to be a foreground interloper. 4XMM J091948.8−121429 does appear to be an excellent ULX candidate associated with the dwarf irregular galaxy PGC 26378, but has only one detection to date with low data quality. The best data set belongs to 4XMM J112054.3+531040 which we find to be a moderately variable, spectrally hard ($\Gamma \approx 1.4$) X-ray source located in a spiral arm of NGC 3631. Its spectral hardness is similar to known PULXs, but no pulsations are detected by accelerated pulsation searches in the available data. We discuss whether other missions provide objects for similar studies and compare this method to others suggested for identifying good PULX candidates.

Key words: X-rays: binaries.

1 INTRODUCTION

Ultraluminous X-ray sources (ULXs; see Kaaret, Feng & Roberts 2017) remain a compelling class of sources to study, despite more than two decades elapsing since the realization that new and exciting astrophysics were required to explain their extraordinary X-ray luminosities of more than 10^{39} erg s^{-1} (e.g. King et al. 2001). In fact, our understanding has evolved substantially from the original focus on ULXs as intermediate mass black hole candidates (IMBHs; Colbert & Mushotzky 1999) to the detection of pulsations in some objects (Pulsating ULXs, or PULXs, e.g. Bachetti et al. 2014). The pulsations reveal the presence of a neutron star (NS) and hence very extreme accretion rates, that can reach apparent factors ∼500 above Eddington (Fürst et al. 2017; Israel et al. 2017a). The observed phenomenology of ULXs is also suggestive of super-Eddington accretion, with the observed X-ray spectra (Gladstone, Roberts & Done 2009; Bachetti et al. 2013), the correlated spectral and temporal variability behaviour (Sutton, Roberts & Middleton 2013b), the detection of fast outflows (Pinto, Middleton & Fabian 2016), and the presence of large bubble nebulae (Pakull & Mirioni 2002) strongly supporting this interpretation; this makes ULXs important to study in the context of the rapid formation of the earliest supermassive black holes (e.g. Bañados et al. 2018). ULXs may also have links with other exotic phenomena; for example, they may constitute an evolutionary phase in the binary stellar systems that ultimately merge and are detected as gravitational wave sources (Mondal et al. 2020a) and may be the systems responsible for Fast Radio Bursts (Sridhar et al. 2021).

The requirement for novel accretion physics is particularly pertinent for explaining ULXs that appear with luminosities in the 10^{40}–10^{41} erg s^{-1} regime, sometimes described as *extreme ULXs*, or eULXs (Gladstone 2013). This is a distinct, separate class from the yet more luminous and rarer hyperluminous X-ray sources (HLXs) that appear above 10^{41} erg s^{-1} and remain the best candidates to host IMBHs, the archetype being ESO 243–49 HLX-1 (Farrell et al. 2009). Given their extreme luminosities, eULXs are relatively well-studied and provide many of the archetypes for ULX behaviour that drive our understanding of it (e.g. Ho IX X-1, Ho II X-1, NGC 5408 X-1, NGC 1313 X-1, etc; see Kaaret et al. 2017 and references therein). Data from such objects has driven many of the breakthroughs in understanding ULXs, from the curvature in their spectra above 2 keV (e.g. Ho IX X-1, Gladstone et al. 2009), to the detection of absorption lines from outflowing gas travelling at $v \approx 0.2c$ (e.g. NGC 1313 X-1, Pinto et al. 2016) and the detection of pulsations indicative of NSs (e.g. M82 X-2, Bachetti et al. 2014). Indeed, the majority of known PULXs reach this regime at their brightest, these being M82 X-2; NGC 1313 X-2 (Sathyaprakash et al. 2019); NGC 7793 P13 (Fürst et al. 2016); and NGC 5907 ULX, which peaks in the HLX regime (Israel et al. 2017a). These luminosities are indicative of NSs with accretion rates at least 50–100 times their Eddington limit.

Many of the current key questions for ULXs relate to PULXs. The demographics of ULXs remain uncertain in terms of the proportion of the overall population that hosts a NS rather than a BH, with

★ E-mail: t.p.roberts@durham.ac.uk

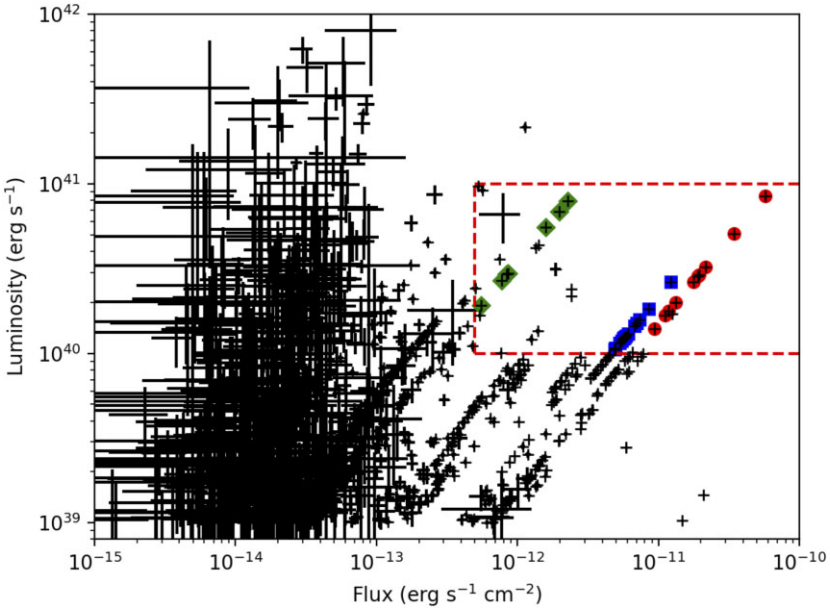

Figure 1. The selection of interesting sources. The high flux, high luminosity region used to select sources is delineated by a dashed red line. Source positions in this parameter space are marked by a black cross, with size matched to the 1σ uncertainties on these quantities (with a minimum cross size adopted for display purposes for those objects with extremely well-constrained values). Three sources are highlighted for appearing multiple times in the region of interest: red circles – M82 X-1; blue squares – NGC 1313 X-1; green diamonds – NGC 5907 ULX. The diagonal tracks are a trivial result of the scaling of flux by distance squared to give luminosity.

some suggestions that NS may dominate (e.g. Koliopanos et al. 2017; Middleton & King 2017; Pintore et al. 2017; Walton et al. 2018). The astrophysics of super-Eddington accretion onto NSs also remains a matter for debate, with the magnetic field strength and configuration (dipole/quadrupole) and the extent to which classical supercritical accretion models apply, in which a geometrically thick inner disc forms and a massive radiation-pressure driven wind is ejected from its surface, all key areas of uncertainty (e.g. Dall'Osso, Perna & Stella 2015; Kluzniak & Lasota 2015; Mushtukov et al. 2015, 2019). A key to progressing all these issues will be to find more PULXs that will add to our population statistics and provide new observations that will help constrain our models of accretion on NS. In this paper, we examine whether the observational quirk that most detected PULXs reach luminosities above 10^{40} erg s^{-1} can be leveraged to find new PULXs, basing our search around the recent large multimission ULX catalogue of Walton et al. (2022) (hereafter W22). The paper is arranged as follows. We discuss the selection of targets in Section 2 and the reduction of the X-ray data for our chosen targets in Section 3. The results are laid out in Section 4 and discussed in Section 5, before the paper is concluded.

2 SOURCE SELECTION

The selection of interesting targets began with our recent multi-mission ULX catalogue, W22, and a simple observation: that four out of six known extragalactic PULXs have been seen to exceed a luminosity of 10^{40} erg s^{-1}. This compares to 1 in 4 ULX detections exceeding this threshold from 4XMM-DR10 and 2SXPS, and 1 in 6 from CSC2.0, in the W22 catalogue. Even more starkly, an integration in the ULX regime, both above and below 10^{40} erg s^{-1}, of the X-ray luminosity function of X-ray binaries in star-forming galaxies from Mineo, Gilfanov & Sunyaev (2012) shows that only 1 in 9 ULXs should appear above this threshold luminosity. However, a bias to high luminosity ULXs in pulsation detections should perhaps be expected, given those detections require photon-rich data, which is more immediately forthcoming from higher luminosity sources at a given distance and exposure length. Nevertheless, this preponderance presents an interesting basis from which to search for new PULXs. We therefore filtered W22 to select ULXs with both a luminosity between 10^{40} and 10^{41} erg s^{-1}, i.e. in the eULX range, and an observed flux sufficiently high that a pulsation detection could be possible given a moderately deep observation, which we set at 5×10^{-13} erg cm^{-2} s^{-1}.[1] We also limit our analysis to *XMM–Newton* data, given that the pn is the only detector currently operating in the 0.5–10 keV band with the combination of effective area and readout time that regularly permits the detection of ULX pulsations (we discuss what similar selection criteria reveal for *Swift* and *Chandra* in Section 5).

We show the flux-luminosity parameter space for the *XMM–Newton* detections in W22 in Fig. 1, with the region of interest delineated. The fluxes used are taken directly from the 4XMM-DR10 EP_8_FLUX column, which is the flux in the broad 0.2–12 keV band (cf. Webb et al. 2020), with the luminosities calculated directly from these fluxes using the distances assumed in W22. Note that there are many other ULX detections at similar fluxes but lower luminosities, which will be the subject of future work. There is also one detection at high flux in the HLX regime; this object will be included in a new study of HLXs (Mackenzie et al., in prep.). In total, 49 detections

[1] PULX detections tend to come from data with $\gtrsim$10 000 pn counts (G. Israel, priv. comm.); at a minimum flux of 5×10^{-13} erg cm^{-2} s^{-1} and a hard, PULX-like spectrum (e.g. power-law continuum with $\Gamma \sim 1.5$ and column $N_{\rm H} \sim 2 \times 10^{21}$ cm^{-2}), this can be obtained in $\sim$100 ks, i.e. within a single *XMM–Newton* orbit, even if we allow for some data loss to background flares (see Section 3). We note that such data sets are rare in the archives for all but a handful of well-studied ULXs; here we focus on analysing the currently available data, with a view to proposing for the necessary observations if any interesting sources are identified.

Table 1. ULXs detected with high flux and high luminosity by *XMM–Newton* in W22.

Source ID (4XMM J. . .)	Host galaxy	d [a] (Mpc)	$L_{\rm X,\,peak}$ [b] ($\times 10^{40}$ erg s^{-1})	# detns [c]	Other name [d]	References [d]
022233.4+422027	NGC 891	9.1	2.40 ± 0.01	1(6)	NGC 891 ULX1	Earley, Dwarkadas & Cirillo (2021), Hodges-Kluck et al. (2012), Wang et al. (2016)
022727.5+333443	NGC 925	8.7	4.5 ± 0.3 (S)	1(1)	NGC 925 ULX-1	Salvaggio et al. (2022), Pintore et al. (2018), Swartz et al. (2011)
031819.9–662910	NGC 1313	4.2	2.8 ± 0.2 (S)	16(29)	NGC 1313 X-1	Pinto et al. (2020), Bachetti et al. (2013), Feng & Kaaret (2006), Colbert & Ptak (2002)
034615.8+681113	IC 342	3.4	1.71 ± 0.01	1(6)	IC 342 X-2	Rana et al. (2015), Mak, Pun & Kong (2011), Roberts, Levan & Goad (2008), Fabbiano & Trinchieri (1987)
072647.8+854550	NGC 2276	39.3	9.9 ± 1.5 (S)	1(1)	NGC 2276 3c	Mezcua et al. (2015), Sutton et al. (2012), Liu (2011)
091948.8–121429	PGC 26 378	26.5	6.6 ± 2.2	1(1)	–	–
095550.4+694045	NGC 3034	3.5	8.50 ± 0.02	10(10)	M82 X-1	Brightman et al. (2020), Pasham, Strohmayer & Mushotzky (2014), Kaaret, Simet & Lang (2006), Matsumoto et al. (2001)
112015.7+133514	NGC 3628	10.5	3.1 ± 0.2 (S)	1(1)	NGC 3628 X-1	Heil, Vaughan & Roberts (2009), Stobbart, Roberts & Wilms (2006), Strickland et al. (2001)
112054.3+531040	NGC 3631	20.1	4.4 ± 1.3 (S)	2(4)	–	Kovlakas et al. (2020), Liu (2011)
131519.5+420301	NGC 5055	9.0	6.7 ± 1.2 (S)	2(2)	NGC 5055 X-1	Mondal et al. (2020b), Berghea et al. (2008), Roberts & Warwick (2000)
143242.2–440939	NGC 5643	16.1	6.0 ± 1.8 (S)	3(3)	NGC 5643 X-1	Kosec et al. (2021), Krivonos & Sazonov (2016), Pintore et al. (2016), Guainazzi et al. (2004)
151558.6+561810	NGC 5907	17.1	11.6 ± 3.2 (S)	7(10)	NGC 5907 ULX1	Fürst et al. (2023), Israel et al. (2017a), Walton et al. (2016), Sutton et al. (2013a)
165251.5–591503	NGC 6221	11.9	3.1 ± 0.3	1(1)	–	–
230457.6+122028	NGC 7479	36.8	9.2 ± 0.4	1(3)	NGC 7479 ULX-1	Earnshaw, Roberts & Sathyaprakash (2018), Sutton et al. (2012) Walton et al. (2011)
235751.0–323726	NGC 7793	3.6	1.5 ± 0.1 (S)	1(9)	NGC 7793 P13	Fürst et al. (2021), Israel et al. (2017b), Motch et al. (2014), Read & Pietsch (1999)

Note. [a] distances are as per adopted by W22. [b] Peak luminosity detected from the ULX, taken from W22. If this is from a *Swift* XRT detection, we add an (S) to the column; no parentheses indicate an *XMM–Newton* detection as there were no peak luminosities observed by *Chandra*. [c] Number of times detected in the high flux, high luminosity regime. Total number of *XMM–Newton* detections in W22 are given in parentheses. [d] Some examples of nomenclature and prior literature for the ULXs are given, but neither is intended as an exhaustive list.

of 15 ULXs are within the interesting parameter space; we list these objects in Table 1. Three objects dominate the detections by number and are highlighted in the figure: M82 X-1 (10 detections), NGC 1313 X-1 (16), and NGC 5907 ULX1 (7). These are amongst the best-studied ULXs (for example, see Table 1), and indeed, the majority of these objects (12/15) are already well-studied in the literature. However, three of the eULXs: 4XMM J091948.8−121429, 4XMM J112054.3+531040, and 4XMM J165251.5−591503 have not been examined in detail before (with 4XMM J112054.3+531040 the only to have been previously catalogued). These three sources are the subject of the remainder of this work.

3 DATA REDUCTION

The primary focus of this work was the data sets in which the catalogued ULX detections were made. These *XMM–Newton* observations, alongside complementary data from *Chandra* and *Swift* where analysed, are listed in Table 2. This also provides an indication of the amount of useful exposure per observation and the count rate detected from each ULX during the observations.

The *XMM–Newton* data were reduced using the science analysis system (SAS)[2] version 20.0.0, with our procedures based largely on the associated analysis threads[3]. All *XMM–Newton* data in Table 2 was taken in full-frame mode in all detectors. We began by reprocessing the data using up-to-date calibration files, and then checked the high-energy (10–12 keV) light curve for each full data set to determine whether background flare filtering was necessary. This was not necessary for any of the data sets for 4XMM J112054.3+531040, where the full-field count rates were always below the suggested nominal cut-off rates for filtering (0.35 ct s^{-1} for the MOS detectors and 0.4 ct s^{-1} for the pn), with the exception of a small number of 100 s pn bins, which only marginally exceeded the threshold and so were retained. In contrast, both data sets for 4XMM J165251.5−591503 required flare filtering, with the standard thresholds used for observation 0405380201 resulting in the loss of ∼10 per cent of the MOS exposure length and ∼50 per cent of that from the pn. The flaring was much more extreme for 0405380901, where standard filters would have resulted in very little exposure surviving; we therefore adopted a much higher threshold for both MOS (2 ct s^{-1}) and pn (10 ct s^{-1}), resulting in the loss of ∼35 per cent of the original MOS data, and up to ∼75 per cent of the pn exposure. The single exposure covering 4XMM J091948.8−121429 was also badly affected by flaring. After the application of the nominal cut-offs, only ∼30 per cent of the MOS exposure was retained, and <20 per cent of that from the pn.

A barycentric correction was applied to the event lists. Light curves and spectra were extracted for 4XMM J112054.3+531040 from a 20-arcsec radius circular aperture centred on the source, with background data extracted from a nearby circular region on the same chip (and at as similar a distance from the read-out nodes as possible in pn data) with radius 40 arcsec. 4XMM J165251.5−591503 was 11–12 arcmin off-axis in each data set and so larger apertures were used, of 30 arcsec radius for the source and 60 arcsec for the background aperture. Similar large apertures were also used for 4XMM J091948.8−121429, which was even further off-axis. All light curves were extracted in the 0.2–10 keV band using events flagged as good (the `#xmmea_em` and `#xmmea_ep` selection criteria for the MOS and pn, respectively). We also selected based on event

[2] https://www.cosmos.esa.int/web/xmm-newton/sas
[3] https://www.cosmos.esa.int/web/xmm-newton/sas-threads

Table 2. Summary of data sets used in this work.

ULX (4XMM J)	Mission	ObsID	Date (YYYY-MM-DD)	Exposure [a] (ks)	Count rate [b] (ct s^{-1})
091948.8–121429	*XMM–Newton*	0694440301	2012-06-07	3.0/7.4/7.1	0.12 [c]
112054.3+531040	*Chandra*	3951	2003-07-05	89.1	48×10^{-3}
	Swift	00034428001 → 00 034 428 026[d]	2016-03-15 → 2016-10-26	42.0	$(6-23) \times 10^{-3}$
	XMM–Newton	0 762 610 401	2016-04-18	6.2/8.5/8.5	0.17
	XMM–Newton	0 762 610 701	2016-04-20	6.2/8.5/8.5	0.18
	XMM–Newton	0 762 610 801	2016-04-22	6.2/8.5/8.5	0.17
	XMM–Newton	0 762 610 501	2016-05-15	18.5/22.4/22.4	0.29
	Swift	00093203001 → 00093203005	2017-09-18 → 2017-10-13	3.2	$<23 \times 10^{-3}$
165251.5–591503 [e]	*XMM–Newton*	0 405 380 201	2007-02-16	8.7/16.6/16.5	$<2.9 \times 10^{-3}$ [f]
	XMM–Newton	0 405 380 901	2007-03-25	6.2/7.3/7.5	0.13 [g]
	Swift	00081199002 → 00081199004	2016-05-24 → 2016-05-26	6.9	$<8 \times 10^{-3}$

Note. [a] Detector live time for central chip of *Chandra* and *XMM–Newton*, or sum of exposures for *Swift*. For *XMM–Newton*, this is shown as pn/MOS1/MOS2, and quoted post-filtering for good time intervals (see text). [b] This is shown for *Swift* as either the range of count rates measured in individual observations (top line), or the upper limit for a sequence with no 3σ detections (lower lines). Note two instances of higher 3σ upper limits – up to $< 31 \times 10^{-3}$ ct s^{-1} – were present in observations in the top line. The *XMM–Newton* count rates are combined across all three EPIC detectors unless otherwise noted, and corrected to the equivalent on-axis count rate. [c] pn-only count rate. [d] There were no observations numbered 00034428006 or 00034428011. [e] The position of 4XMM J165251.5−591503 was covered by a third observation, 0690580101, but the position of the ULX candidate was at the edge of the field of view and no detection of it was present from this data set in 4XMM-DR10. We therefore do not analyse this data. [f] 3σ upper limit for aperture photometry for combined MOS1 and MOS2 data. [g] Combined MOS1 and MOS2 count rate.

pattern, with a threshold of $\leq$4 for pn data (single and double events) and $\leq$12 for MOS (which also includes triples and quadruples). We used EPICLCCORR to subtract background counts and correct the light curves for instrumental effects such as vignetting and deadtime, and where we co-added light curves over the three different detectors, we ensured the light curves had the exact same start and stop times (taken from the pn data). Spectra were extracted using the same patterns and flags as the light curves, except that the more stringent FLAG = 0 was used for the pn. Response matrices (rmf files) and ancillary response files (arf) were produced for each spectrum, with the latter incorporating a correction so the spectra better align with *NuSTAR* calibration. Finally, the spectra were binned to a minimum of 25 counts per bin and with an oversampling factor limited to three times the intrinsic energy resolution of the detector across all photon energies.

The *Swift* data utilized in the analysis of 4XMM J112054.3+531040 were all obtained directly from online tools associated with the 2SXPS catalogue[4] (Evans et al. 2020). The stacked spectrum, composed of all XRT data for the ULX, was obtained directly from the 2SXPS interface, which also provided appropriate background data and response (rmf and arf) files. The spectral data were binned to 20 counts per bin before fitting. The *Swift* data points contributing to the full light curve were extracted on the basis of one point per observation, with the data either displayed as a detection (with corresponding 1σ error), where the count rate exceeded three times the error, or as a 3σ upper limit in other cases.

We also include the analysis of an archival *Chandra* data set for 4XMM J112054.3+531040. We reduced this data using the *Chandra* interactive analysis of observations software package, CIAO[5] version 4.14, and version 4.9.8 of the *Chandra* calibration data base. Our reduction again relied heavily on the provided science threads[6]. The data was reprocessed and data products for the ULX were extracted from an 8-pixel (∼4 arcsec) radius aperture centred on the source. Given the proximity of a second, much fainter source (about 7 arcsec to the south-west), we chose to use a separate background region rather than an annulus, which we set as a 20-pixel circular aperture to the north-west of the ULX. We then extracted the source and background spectra, and corresponding response files, using the SPECEXTRACT tool, and grouped the output spectra to a minimum of 20 counts per bin before analysis. The events file was barycentre-corrected, and then background-subtracted light curves were extracted using the same regions and the DMEXTRACT tool. Finally, we attempted to produce an improved position for 4XMM J112054.3+531040 by correcting the astrometry of the *Chandra* data to corresponding optical counterparts in the *Gaia* DR2 catalogue (see Section 4.2.3 for more details).

4 RESULTS

4.1 4XMM J091948.8−121429

This candidate ULX is associated with the dwarf galaxy PGC 26 378 (also known as DDO 060 or MCG -02-24-011) at a distance of 26.5 Mpc (W22). It appears co-located with a knot of emission about 30 arcsec north of the nominal centre of the host galaxy, as shown in Fig. 2. It is only detected by *XMM–Newton* and inspection of the reduced data of the single observation covering its position reveals it to lie at the very edge of the pn field of view, at ∼16 arcmin off-axis. It was not detected in either MOS image given that the 'good' event flags filter used to clean the data rejected events so far off-axis. Hence, only 3 ks of pn data for this source were available for analysis,

[4] https://www.swift.ac.uk/2SXPS/
[5] https://cxc.harvard.edu/ciao/index.html
[6] https://cxc.harvard.edu/ciao/threads/index.html

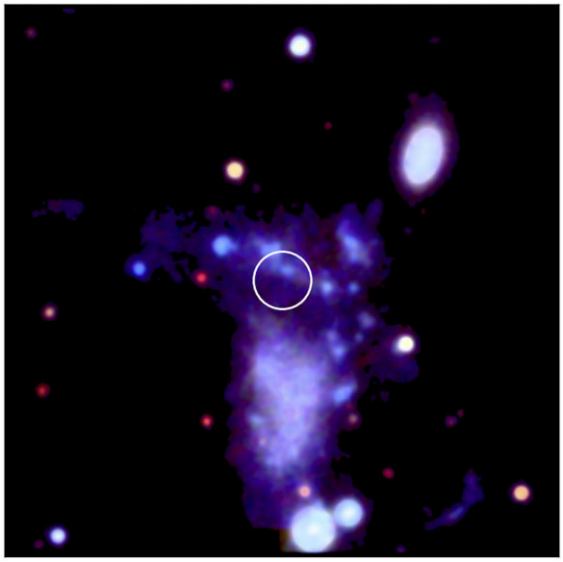

Figure 2. The environment of 4XMM J091948.8−121429 shown as a three-colour PanSTARRs image. The red, green, and blue colours represent light observed in the *i*, *r*, and *g* filters, respectively. The data in each filter is convolved with a 2-pixel (≡ 0.5 arcsec) Gaussian kernel for display purposes. A circle of radius 6.25 arcsec marks the 3σ error in the position of the ULX as determined in 4XMM-DR10, and the field of view is 2×2 arcmin^2. The PanSTARRs data was obtained from http://ps1images.stsci.edu/cgi-bin/ps1cutouts.

from which we had <100 source counts[7]. Strong constraints on the source properties and behaviour are therefore not possible without obtaining further data.

However, we were able to obtain some provisional constraints on the ULX properties by analysing its pn spectrum. In particular, we extracted the spectrum and then binned it only on the oversampling parameter, such that we did not oversample the energy resolution (precisely as per other *XMM–Newton* spectra analysed in this work); we did not specify any minimum number of counts per bin. This spectrum was then fitted in XSPEC[8] using Cash statistics. We report the results for two simple models – an absorbed power-law continuum, and an absorbed multicolour disc blackbody spectrum – in Table 3. The fits assumed a Galactic foreground column of 4.85×10^{20} cm^{-2}, interpolated from Dickey & Lockman (1990) using the COLDEN interface[9]. Here and throughout this paper, we use the TBABS model for absorption (Wilms, Allen & McCray 2000). We find the spectrum to be relatively hard ($\Gamma \sim 1.6$ or $kT_{\rm in} \sim 1.9$ keV), albeit with a very wide range of possible photon indexes or disc temperatures, and with a relatively low intrinsic absorption for a ULX ($\lesssim 6 \times 10^{20}$ cm^{-2}). The estimated flux is $\sim 4 \times 10^{-13}$ erg cm^{-2} s^{-1}, again with a wide uncertainty range, which equates to a 0.3–10 keV luminosity of $\sim 3 \times 10^{40}$ erg s^{-1} at the distance of PGC 26378.

[7]Given the low detected count rate and severe flaring, taking a higher threshold for the background filtering resulted in background domination at high and low energies, e.g. below 0.5 and above 4 keV for the 10 count s^{-1} GTI filter used for 4XMM J165251.5−591503. The resulting spectral constraints were no better than those from the method detailed in the text.

[8]Version 12.12.1, available as part of the HEASOFT package from https://heasarc.gsfc.nasa.gov/docs/software/heasoft/. Throughout this work, we adopt the convention of quoting 90 per cent errors on spectral fitting results.

[9]https://cxc.harvard.edu/toolkit/colden.jsp

Table 3. Single component spectral model fits for 4XMM J091948.8–121429.

$n_{\rm H}$ [a]	$\Gamma/kT_{\rm in}$ [b]	$f_{\rm X}$ [c]	C-stat/dof [d]
power-law continuum			
$0.30^{+0.34}_{-0.25}$	$1.6^{+0.8}_{-0.6}$	$4.1^{+2.5}_{-1.6}$	29.7/37
multicolour disc blackbody			
<0.35	$1.9^{+4.8}_{-0.8}$	$3.7^{+1.3}_{-1.4}$	31.2/37

Note. [a] Absorption in excess of foreground Galactic ($\times 10^{21}$ cm^{-2}). [b] Photon index for power-law or inner-disc temperature (in keV) for disc blackbody. [c] Observed 0.3–10 keV flux, corrected for foreground Galactic absorption ($\times 10^{-13}$ erg cm^{-2} s^{-1}). [d] C-statistic value and number of degrees of freedom for fit.

4.2 4XMM J112054.3+531040

This ULX candidate has the richest data set of the three we examine in the section, with data from all three missions covered by the W22 catalogue. We separate out the more detailed analysis this facilitates into three sections below.

4.2.1 X-ray spectra

The spectra for 4XMM J112054.3+531040 were all extracted and binned as detailed in Section 3. After background subtraction they had sufficient counts to permit fitting using the χ^2 statistic. In this analysis, the *XMM–Newton* and *Swift* data were fitted in the 0.3–10 keV band, and the *Chandra* data were fitted in the narrower 0.5–8 keV regime commensurate with its more limited spectral response. As an initial step, the data were all fitted separately with simple power-law continuum and multicolour disc blackbody models. For each spectrum, we included a foreground absorption component set to 1.02×10^{20} cm^{-2}, derived from COLDEN as above. We also included a constant component for each *XMM–Newton* observation to model slight calibration differences between the detectors; in practise, differences in this component between detectors never exceeded 15 per cent for any individual observation. The results of these fits are displayed in Table 4. It is immediately obvious that this ULX is relatively hard, with a photon index Γ that does not deviate substantially from 1.4, and with moderate absorption beyond our own Galaxy (and so likely to be intrinsic to the ULX or its host galaxy) of $\lesssim 10^{21}$ cm^{-2}; the equivalent parameters for the disc blackbody model are $kT_{\rm in} \sim 2$ keV and negligible column in excess of Galactic. The power-law provides a statistically-acceptable fit to all spectra; however, this is not the case for all disc-blackbody fits, with *XMM–Newton* observations 0762610801 and 0762610501 not providing acceptable fits (null hypothesis probability <5 per cent). We also show a flux for each observation, which is the observed flux corrected only for foreground Galactic absorption, as calculated using the CFLUX convolution model in XSPEC. The ULX does appear to vary in flux, albeit only by a factor ∼2 between different observations.

Given the similarity of the spectral parameters across all of the X-ray observations, we attempted to fit all the spectra simultaneously with the same power-law model, allowing only the relative constant differences between the *XMM–Newton* detectors to vary. This did not produce a good fit to the data when the normalization of the power-law continua were all constrained to the same value ($\chi^2 = 681.5$ for 391 degrees of freedom). However, permitting the normalizations to vary (and so the flux of the source to vary between epochs) produced a substantial improvement of $\Delta\chi^2 = 278$ for 5 fewer degrees of freedom, and a statistically-acceptable fit to the data. Further unfreezing of fit parameters did not result in large statistical

Table 4. Single component spectral model fits.

ObsID	$n_{\rm H}$ [a]	$\Gamma/kT_{\rm in}$ [b]	$f_{\rm X}$ [c]	χ^2/dof [d]
power-law continuum				
3951	$1.24^{+0.38}_{-0.36}$	1.38 ± 0.08	5.5 ± 0.3	130/144
Swift stack	<1.62	$1.21^{+0.26}_{-0.17}$	$5.4^{+0.8}_{-0.9}$	19/16
0762610401	$1.30^{+0.84}_{-0.72}$	$1.57^{+0.19}_{-0.17}$	$3.6^{+0.4}_{-0.5}$	34/27
0762610701	<1.22	$1.23^{+0.16}_{-0.15}$	$4.4^{+0.6}_{-0.5}$	16/29
0762610801	<1.13	$1.46^{+0.17}_{-0.15}$	$3.5^{+0.6}_{-0.4}$	36/29
0762610501	$0.83^{+0.23}_{-0.21}$	1.45 ± 0.06	$6.5^{+0.3}_{-0.5}$	128/127
multicolour disc blackbody				
3951	<0.14	$1.90^{+0.14}_{-0.12}$	4.6 ± 0.2	139/144
Swift stack	<0.58	$2.09^{+0.62}_{-0.4}$	4.4 ± 0.7[e]	17/16
0762610401	<0.38	$1.52^{+0.22}_{-0.19}$	3.0 ± 0.4	34/27
0762610701	0[f]	$2.16^{+0.41}_{-0.3}$	3.7 ± 0.5	21/30
0762610801	0[f]	$1.62^{+0.24}_{-0.2}$	3.0 ± 0.4	50/30
0762610501	$<2.7 \times 10^{-2}$	$1.87^{+0.11}_{-0.10}$	5.8 ± 0.3	194/127

Note. [a] Absorption in excess of foreground Galactic ($\times 10^{21}$ cm^{-2}). [b] Inner disc temperature is in keV. [c] Observed 0.3–10 keV flux, corrected for foreground Galactic absorption ($\times 10^{-13}$ erg cm^{-2} s^{-1}). [d] χ^2 value and number of degrees of freedom for fit. [e] Absorption fixed at 0 in order to obtain error range.

Table 5. Single component fits for 4XMM J112054.3+531040 with parameters constrained to the same value across all spectra.

$n_{\rm H}$ [a]	$\Gamma/kT_{\rm in}$ [b]	χ^2/dof [c]
power-law continuum		
0.92 ± 0.15	1.42 ± 0.04	403.6/386
multicolour disc blackbody		
0[f]	1.86 ± 0.07	470.8/387

Note. [a] Absorption in excess of foreground Galactic ($\times 10^{21}$ cm^{-2}). [b] Photon index for power-law or inner-disc temperature (in keV) for disc blackbody. [c] χ^2 value and number of degrees of freedom for fit. [f] Value fixed to zero as model does not require any additional absorption.

improvements – a small but not very significant improvement of $\Delta\chi^2 = 22$ for 5 fewer degrees of freedom resulted from thawing the photon index, and minimal improvement resulting from thawing the absorption component ($\Delta\chi^2 = 6$ for 5 fewer degrees of freedom). We therefore conclude that there is no strong evidence for variability in either the absorption component or the spectral shape throughout the observations. We present the best-fitting power-law and disc-blackbody parameters, where absorption and photon index/inner-disc temperature are constrained to the same values across all spectra, in Table 5. Note that the disc-blackbody model is not statistically acceptable as a result of the two individual spectra noted above; it also does not require any absorption above Galactic foreground in its best fit.

We also consider two-component fits to the spectra, composed of two thermal components, consistent with modelling of good quality 0.3–10 keV ULX spectra (e.g. Stobbart et al. 2006; Koliopanos et al. 2017). In order that we can potentially place meaningful constraints, we must use only the best quality examples of the spectra of 4XMM J112054.3+531040, which means the *Chandra* spectrum and the 0762610501 *XMM–Newton* spectrum (both of which have in excess of 100 bins). In addition, we note that the other three *XMM–Newton* spectra have similar levels of flux and spectral parameters (Table 4), and were obtained within a 5-day window in 2016 (Table 2). We therefore consider them suitable for combining a single spectrum per *XMM–Newton* detector, and to do so, we used the SAS tool EPICSPECCOMBINE to combine the data across the three observations, before binning as previously described. This had similar spectral quality to the other two data sets and so we used it in the two-component spectral fitting.

Given the similarities of the individual data sets discussed above, we also adopted a simultaneous fitting process for the three higher quality spectra. An initial fit held all values (other than the corrections for relative EPIC detector calibrations) fixed across the three spectra, and a statistically poor fit resulted $\chi^2 = 652$ for 377 degrees of freedom). Thawing the normalizations of the hot and cool disc blackbody components both resulted in significant improvements to the fits, with $\Delta\chi^2 = 247$ and 27 (for 2 fewer degrees of freedom) for the hot and cool components, respectively, when applied consecutively. However, thawing the disc temperatures and the absorption did not result in any further, additional improvements to the fits ($\Delta\chi^2 \leq 5$ for 2 degrees of freedom), so we keep those values the same across all three data sets. The resulting fit is shown in Table 6, where we also show the intrinsic fluxes of each disc blackbody component (as calculated using CFLUX). The absorption and disc component temperatures are within the range of values observed from bright ULXs (cf. Koliopanos et al. 2017; Walton et al. 2018), albeit towards the harder end of the range. The ratio between the flux in either component is rather high, and interestingly may vary between the *Chandra* observation in 2003 and the *XMM–Newton* observations in 2016, with $f_{\rm X,2}/f_{\rm X,1} = 10 \pm 4$ in the earlier epoch, and $(6-7) \pm 3$ in the latter (note these are 90 per cent and not 1σ errors). We illustrate these fits in Fig. 3, where we show the unfolded spectra and both underlying model components.

4.2.2 *X-ray variability*

We have composed a long-term light curve for 4XMM J112054.3+531040 from the archival *XMM–Newton*, *Chandra*, and *Swift* data, which we display in Fig. 4. The *XMM–Newton* and *Chandra* fluxes were taken directly from the individual power-law spectral fits and converted to a luminosity for a distance of 20.1 Mpc; the *Swift* fluxes were calculated based on a conversion factor of $1\,{\rm ct\,s^{-1}} \equiv 5.65 \times 10^{-11}$ erg cm^{-2} s^{-1}, derived from the best fit spectral model in the PIMMS[10] calculator. The light curve shows that 4XMM J112054.3+531040 is moderately variable on time-scales of days (up to factors of $\sim$5 in *Swift* data), but has remained luminous in all observations to date with $L_{\rm X}$ (0.3–10 keV) persistently $>10^{40}$ erg s^{-1}. However, coverage is limited, with most observations in a short window in 2016 as the *XMM–Newton* and *Swift* observations were a follow-up programme for a supernova, AT2016bau (see Arbour 2016; Granata et al. 2016). The supernova lies $\sim$45 arcsec from the ULX, in the direction of the centre of the host galaxy (cf. Fig. 7), and remained undetected in the *XMM–Newton* and *Swift* data. We note the only period of observations without a detection were the five follow-up observations with *Swift* in late 2017. These observations were short and so do not provide stringent individual limits; however, combining their data provides a 3σ upper limit on the luminosity of $<2.05 \times 10^{40}$ erg s^{-1} for that period, similar to the lowest detected luminosities from a year earlier.

We also investigated the intra-observational variability in the *XMM–Newton* and *Chandra* data. In Fig. 5, we show summed EPIC light curves for all four *XMM–Newton* observations. In each case,

[10] https://cxc.harvard.edu/toolkit/pimms.jsp

Table 6. Two component spectral fits for 4XMM J112054.3+531040.

ObsID	$n_{\rm H}$ [a]	$kT_{\rm in,\,1}$ [b]	$kT_{\rm in,\,2}$ [b]	$f_{\rm X,\,1}$ [c]	$f_{\rm X,\,2}$ [c]	χ^2/dof [d]
3951	–	–	–	0.5 ± 0.2	4.8 ± 0.2	–
Combined (401 + 701 + 801)	$0.29^{+0.29}_{-0.24}$	$0.48^{+0.17}_{-0.11}$	$2.69^{+0.54}_{-0.3}$	$0.5^{+0.2}_{-0.1}$	$3.2^{+0.2}_{-0.3}$	377.8/373
0762610501	–	–	–	$0.8^{+0.3}_{-0.2}$	5.5 ± 0.4	–

Note. Where a value is shown solely in the middle row, it is the result of a simultaneous fit to all three data sets. [a] Absorption in excess of foreground Galactic ($\times 10^{21}$ cm^{-2}). [b] Inner-disc temperature (in keV) for disc blackbody components. [c] Intrinsic flux of component in 0.3–10 keV band ($\times 10^{-13}$ erg cm^{-2} s^{-1}); this value is extrapolated beyond the fitted energy range for the *Chandra* data. [d] χ^2 value and number of degrees of freedom for fit.

we limit the light curves to the pn start and stop times to ensure simultaneity across the three EPIC detectors, and bin the data to 500 s intervals. Visual inspection of Fig. 5 hints that the data might vary in excess of that expected from white noise processes, and this is confirmed by calculating the excess variance ($\sigma_{\rm XS}$; see Vaughan et al. 2003) for each data set, which in each case is in the range 4–9 per cent. We performed the same analysis on the *Chandra* data set, binned to 1000 s given its lower count rate, and found a similar $\sigma_{\rm XS} = 7$ per cent; we show this light curve in Fig. 6. This demonstrates that 4XMM J112054.3+531040 is consistently varying on time-scales as short as <10 min.

In order to investigate variability at the shortest accessible time-scales, we used the the STINGRAY packages (Huppenkothen et al. 2019; Bachetti et al. 2022), as scripted up in the HENDRICS tools[11]. We worked on the *XMM–Newton* EPIC-pn data as its 73.4 ms frame time means it is the only data for 4XMM J112054.3+531040 with the time resolution adequate to access the ∼1 Hz pulsations seen in PULXs. We extracted pn event files from the source apertures for each *XMM–Newton* observation, and performed barycentric corrections on each event list. We first used these event files to create power spectra for each observation. Each power spectrum was subject to geometric rebinning over a variety of factors in the range 0.01–0.3 before inspection; however, there was no power above the white noise level in any of the power spectra, which were sensitive to power in the $\sim 10^{-3}$–6 Hz range. (We note this is consistent with the excess variance results above, which are based on variability over longer time-scales than probed by the power spectra.) We then performed accelerated pulsation searches using the HENDRICS implementation of the Ransom, Eikenberry & Middleditch (2002) algorithm. Although each search found candidate pulsations, these were statistically weak (highest powers in the range 30–40), and were generally not recovered by Z^2_N searches focussing on a narrow range around the candidate frequency, so we do not regard any as real pulsation candidates. This Z^2_N test was used to place limits on the amplitude of possible pulsations in the data; for the shorter (∼6 ks in the pn) observations, the 3σ upper limit on the possible pulsation amplitude at frequencies $\gtrsim$1 Hz was ∼45 per cent, and for the longer (18 ks, 0762610501 data set) a more stringent limit on the pulsation amplitude of ∼20 per cent at similar frequencies was calculated.

4.2.3 *Optical follow-up*

An accurate position for 4XMM J112054.3+531040 was obtained from the *Chandra* data by considering matches between X-ray source detections on the S3 chip and optical sources from *Gaia* DR2, as per the relevant science thread[12]. The best solution was obtained from the raw data; any attempts to correct the astrometry algorithmically induced false matches within the body of NGC 3631, which resulted in no good matches in the field and an overall matching error >0.6 arcsec. If we used the raw data, we would instead have found three excellent matches and a statistical error of 0.14 arcsec on the field astrometry. Using this astrometric solution, we find a J2000 position for the eULX of 11 20 54.306, +53 10 40.68 ± 0.02 arcsec (X-ray centroid error), ±0.14 arcsec (astrometric uncertainty).

We then investigated the environment and possible counterparts of 4XMM J112054.3+531040 using *HST* data. Specifically, the eULX position was covered by three *HST* images. A pair of WFC3 UVIS images, in the *F*555*W* and *F*814*W* filters, each of ∼750 s exposure (data sets ID9610010 & ID9610020), were taken in October 2016 and aimed at SN AT2016bau, as per most of the X-ray data; and a deeper ∼2300 s ACS WFC image was taken in April 2019, also in the *F*814*W* filter (data set JDXK07010). We display the latter, with the ULX position highlighted in a zoom of its projected immediate vicinity, in Fig. 7. 4XMM J112054.3+531040 clearly lies in a spiral arm to the west of the nucleus of NGC 3631 and is associated with some structure within the arm, consistent with it being a *bona fide* eULX rather than a background AGN.

Fig. 7 shows two relatively bright sources within the 3σ uncertainty region and a third just outside. The central source appears to be potentially extended towards the south-east, so may be an amalgamation of two (or more) objects. The Hubble source catalogue (Whitmore et al. 2016)[13] provides magnitudes in both filters from the 2016 WFC3 UVIS observation; both objects within the error region have near-identical magnitudes of $m_{\rm F555W} = 23.86/23.87$ and $m_{\rm F814W} = 23.68/23.66$, for the central and north-western objects, respectively, and hence both have a colour $m_{\rm F555W} - m_{\rm F814W} \approx 0.2$. The object to the east of the error region is very slightly brighter, with $m_{\rm F555W} = 23.36$, $m_{\rm F814W} = 23.51$, and so a colour of $m_{\rm F555W} - m_{\rm F814W} = -0.15$. After correcting for minimal foreground extinction from within our own Galaxy, absolute magnitudes of $M_{\rm F555W} \approx -7.7$ and $M_{\rm F814W} \approx -7.5$ can be calculated for the two most likely counterparts. This combination of absolute magnitude and slightly red colour is not a good match for any type of supergiant star, but may perhaps instead be indicative of young stellar clusters in NGC 3631, with the possibility of some reddening due to local dust extinction in the spiral arm. It is also likely that the observed magnitudes of these counterparts rule out a background AGN, given that these typically have $f_{\rm X}/f_{\rm opt} \sim 0.1$–10 (e.g. Aird et al. 2010), whereas $f_{\rm X}/f_{\rm opt} > 220$ for this eULX.

[11] Version 7.0, see https://hendrics.stingray.science/en/stable/index.html.
[12] https://cxc.cfa.harvard.edu/ciao/threads/reproject_aspect/
[13] https://catalogs.mast.stsci.edu/hsc/

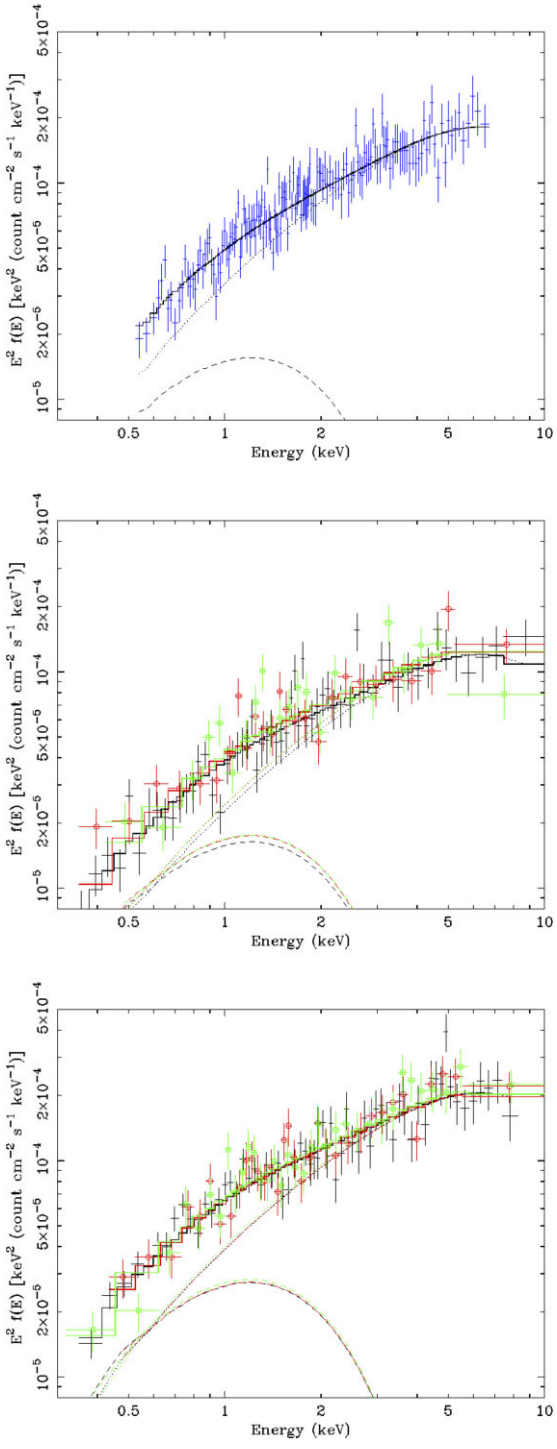

Figure 3. Unfolded two-component spectral fits for 4XMM J112054.3+531040. (*Top*) *Chandra* spectrum, with data points shown as crosses (in blue). The best fitting model is the solid line, and the hot and cool disc components are shown as dotted and dashed lines, respectively. (*Middle*) Combined spectral data from *XMM–Newton* observations 07262610401, 0762610701, and 0762610801. Model components are indicated as per the top panel (with the slight offsets from the different constants in the modelling). Data from the pn is shown as simple crosses (in black), MOS1 is highlighted by a circle (red) and MOS 2 by a square (green). (*Bottom*) Data from *XMM–Newton* observation 0762610501, displayed similarly to the middle panel.

4.3 4XMM J165251.5−591503

The position of 4XMM J165251.5−591503 has been covered by three *XMM–Newton* observations, but only one (ObsID 0405380901) provided a reasonably high source count rate, and this observation was heavily affected by flaring (cf. Table 2 and Section 3). Worse still, the source lay at the very edge of the pn detector, where a sizeable fraction of the source extraction aperture lay outside the field of view; we therefore concentrated our analysis on the MOS detections of this source, where the flare contamination was also less pronounced than for the pn. Spectra were extracted and fitted with simple single-component models, similarly to the previous sources. We report the results of this analysis in Table 7. In this case, the foreground column was higher, at 1.53×10^{21} cm^{-2}. We find the source to display a relatively soft spectrum, with $\Gamma \sim 2.5$ for a power-law continuum, or $kT_{\rm in} \sim 0.65$ keV for a multicolour disc blackbody model. The latter shows no evidence for absorption above the Galactic line of sight. Both models provide formally acceptable fits to the data, although the χ^2 is better for the power-law model. The source flux (corrected for Galactic absorption) is the highest for any of our three new eULX candidates at $\sim 10^{-12}$ erg cm^{-2} s^{-1}. However, this is not a persistent flux; we note that the upper limit on the count rate from a second observation (taken roughly 5 weeks prior to the data set fitted above) was a factor ∼45 lower, so this object is strongly X-ray variable on a time-scale of weeks.

This variability is corroborated by *Swift* data; the position of 4XMM J165251.5−591503 is covered by three *Swift* observations (as listed in Table 2, the target for which was NGC 6221), taken over 3 days in 2016 and totalling 6.9 ks of exposure. No source is detected at the ULX position in 2SXPS analysis of this data. We have therefore performed aperture photometry at the position of the source and find a combined 3σ upper limit on the flux as $\lesssim 2 \times 10^{-13}$ erg cm^{-2} s^{-1} (converting the upper limits on the count rate to flux in PIMMS using the power-law spectrum in Table 7). Although not as constraining as the second *XMM–Newton* observation, this again highlights that this object is variable and, nine years after the original detection, it had a factor ≥5 lower flux compared to the earlier epoch.

The high foreground column is indicative that the line of sight to this eULX candidate lies close to the Galactic plane. In fact, its Galactic coordinates are $l_{\rm II} = 329.72$, $b_{\rm II} = -9.60$, which lie both close to the Galactic plane and near the direction of the Galactic Centre. This, combined with the soft spectrum, lead to a suspicion that this could be a foreground Galactic source. We therefore conducted a more extensive check for multi-wavelength counterparts and found that 4XMM J165251.5−591503 has a bright IR counterpart, detected within ∼1 arcsec of the eULX candidate position, with $m_{\rm K} = 13.01 \pm 0.03$ in the 2MASS all-sky point source catalogue (Cutri et al. 2003). Given this strongly suggests a Galactic counterpart, we also checked *Gaia*-DR3 (Gaia Collaboration 2022), and found the counterpart with $m_{\rm g,mean} = 15.6$ and a parallax of 0.41 ± 0.03 mas. The presence of a parallax means that this counterpart is clearly Galactic, and the measured value places it at a distance of 2.4 ± 0.2 kpc. The apparent magnitude of the counterpart then converts to a mean absolute magnitude of $M_{\rm g} \approx 3.2$, correcting for foreground extinction of $A_{\rm g} = 0.5$ (Schlafly & Finkbeiner 2011, via the NASA/IPAC extragalactic data base[14]), and the 0.3–10 keV X-ray luminosity is $L_{\rm X} \approx 7 \times 10^{32}$ erg s^{-1}.

To investigate its nature further, we extracted a *TESS* light curve at its position. *TESS* observed the target during Sector 12 (2019-May-

[14] https://ned.ipac.caltech.edu

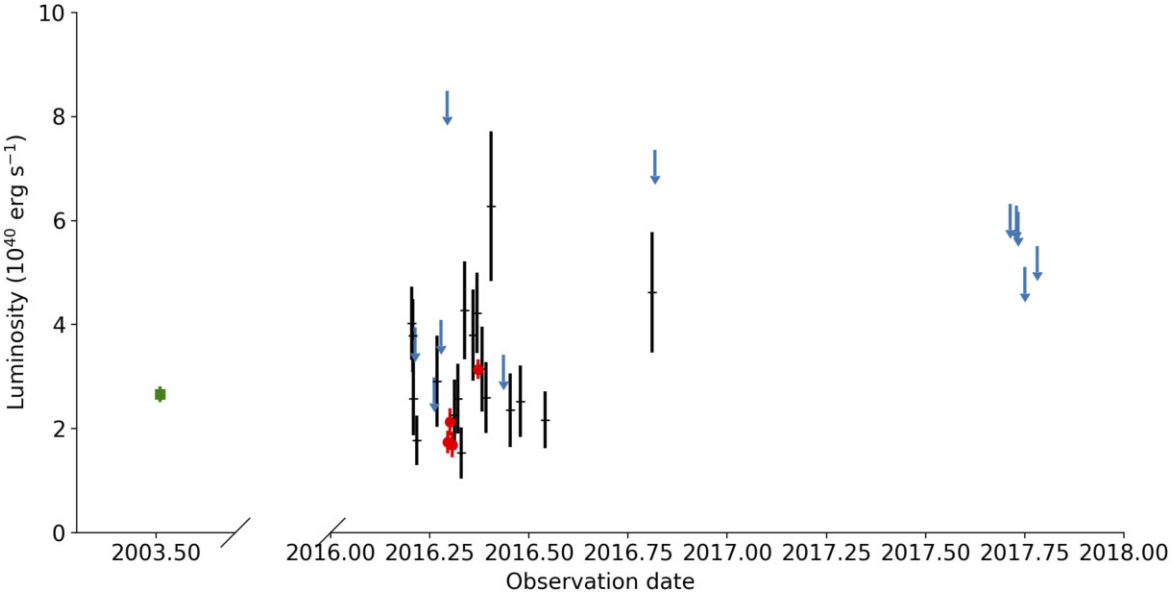

Figure 4. Long-term light curve for 4XMM J112054.3+531040 from all missions. The *Chandra* observation is shown as a (green) square, *XMM–Newton* observations are (red) circles, *Swift* 3σ detections are black crosses, and 3σ upper limits from *Swift* are (blue) downward arrows. Note that the *x*-axis is broken for display purposes, given the long (13 yr) gap between the *Chandra* and subsequent observations.

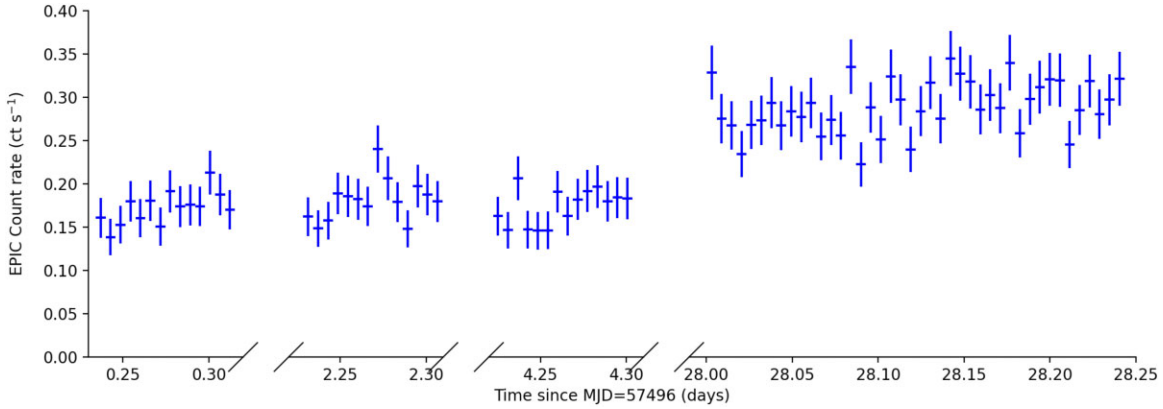

Figure 5. Combined EPIC light curves for 4XMM J112054.3+531040 from each individual exposure, displayed with 500 s binning. Note that the *x*-axis is broken for display purposes.

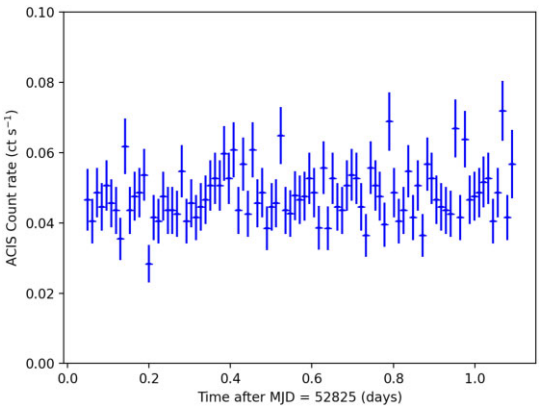

Figure 6. *Chandra* ACIS-S light curve for 4XMM J112054.3+531040 shown with 1000 s binning.

21 to 2019-Jun-19) at 30 min cadence. We extracted its light curve by defining target and background apertures around the target and show the resulting light curve in Fig. 8. The counterpart displays a clear ∼2-d modulation on top of a possible longer term variation. Given the *Gaia* distance and colour, the position in the *Gaia* calibrated colour-magnitude diagram places this system as a K-type star, with its absolute magnitude suggesting an evolved type. It may therefore be possible that the 2-d modulation is related to the orbital period of a binary, with the X-ray emission potentially originating in colliding winds. Alternatively the optical variability could be related to a superorbital modulation caused by a precessing tilted disc, as observed in several cataclysmic variables (see, e.g. Hkiewicz et al. 2021); however, it is unclear what the origin of the X-ray emission might be in this scenario. A third possible scenario is unrelated to the possible binary nature of the stellar system; this may simply be a stellar flare. At close to 10^{33} erg s^{-1}, this would be at the upper end of known flare luminosities (cf. Table 4 of Güdel 2004), and the ratio of quiescent to flare luminosity would also be rather extreme

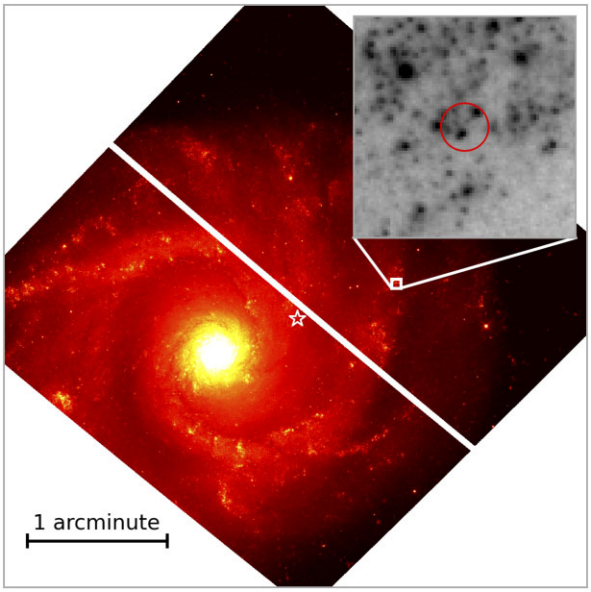

Figure 7. *HST* ACS WFC image of NGC 3631 in the *F*814*W* filter (main image, using a heat colour map). The image is aligned such that North is up, and East to the left. The location of 4XMM J112054.3+531040 is within the small white box, and the region within the box is shown in detail in the insetted zoom, which has size 4 × 4 arcsec^2 and is displayed as a grey-scale image. The position of the eULX is highlighted by the red circle, which is equivalent to the 3σ error region for the eULX position. The position of SN2016bau is highlighted by the white star.

Table 7. Single component fits for 4XMM J165251.5−591503.

$n_{\rm H}$ [a]	$\Gamma/kT_{\rm in}$ [b]	$f_{\rm X}$ [c]	χ^2dof [d]
power-law continuum			
$2.0^{+1.5}_{-1.2}$	$2.5^{+0.5}_{-0.4}$	$1.1^{+0.3}_{-0.2}$	54.4/50
multicolour disc blackbody			
0[f]	$0.65^{+0.13}_{-0.1}$	$0.9^{+0.1}_{-0.2}$	66.2/51

Note. [a] Absorption in excess of foreground Galactic ($\times 10^{21}$ cm^{-2}). [b] Photon index for power-law or inner-disc temperature (in keV) for disc blackbody. [c] Observed 0.3–10 keV flux, corrected for foreground Galactic absorption ($\times 10^{-12}$ erg cm^{-2} s^{-1}). [d] χ^2 value and number of degrees of freedom for fit. [f] Value fixed to zero as model does not require any additional absorption.

for a late stellar type (Pye et al. 2015), but this is a plausible nature given its soft X-ray spectrum. It is even possible that this optical counterpart is entirely unrelated to the X-ray emission, which still might be originating in a *bona fide* ULX in NGC 6221. The nature of this source therefore remains to be confirmed and will require follow-up observations to resolve.

5 DISCUSSION

5.1 Have we found any good PULX candidates?

In this paper, we have identified and studied three new extreme ULX candidates, selected on the basis of at least one high flux ($>5 \times 10^{-13}$ erg cm^{-2} s^{-1}) and high luminosity ($L_{\rm X} > 10^{40}$ erg s^{-1}) *XMM−Newton* detection in the ULX catalogue of W22, with a view to identifying good PULX candidates. So, what have we learnt?

The first object, 4XMM J091948.8−121429, has insufficient data to determine whether it is a good candidate to be a PULX. Its host is relatively distant at 26.5 Mpc, and its only detection is 16 arcmin off-axis in 3 ks of cleaned pn data, so <100 counts were obtained from the source. This was, however, sufficient to determine that the object appears likely to be within its host given its association with structure in PGC 26378, and that its spectrum is likely to be moderately hard (although this is poorly constrained). It is pertinent to note that the host galaxy is a dwarf irregular system; several such systems are known to host eULXs, including some of the best studied local objects (e.g. NGC 5408, Holmberg II). Indeed, some of these objects are particularly interesting as local analogues for processes at high redshift, e.g. I Zw 18 (Kaaret & Feng 2013) and Haro II (Prestwich et al. 2015). So, 4XMM J091948.8−121429 is at least a good candidate for a *bona fide* eULX, but further observations are required to reveal the details of this interesting object.

4XMM J112054.3+531040, in contrast, has a reasonable set of data already available, largely thanks to the follow-up of a supernova that detonated in the host galaxy, NGC 3631, in 2016. This includes over 40 ks of *Swift* snapshots, four short *XMM–Newton* observations, and a much earlier (2003) and deeper *Chandra* observation. These reveal a source that varies in flux by a factor ∼2–3 on time-scales from days to years and that has demonstrable variability on time-scales as short as tens of minutes. Its spectrum is generally hard for a ULX, represented by a power law with $\Gamma \sim 1.4$; however, it can also be satisfactorily described by a two-component model with both components being thermal in nature, with the form and its parametrization within the known range of spectra for ULXs. Combining *Chandra* astrometry with *HST* imaging reveals possible counterparts to the ULX within a spiral arm of the host that have colour and magnitude similar to young stellar clusters, but far too high an X-ray/optical flux ratio for a background AGN. It therefore is a good eULX detection, and its hardness marks it out as a good PULX candidate given that PULXs tend to have harder-than-average X-ray spectra amongst ULXs, generally due to the dominance of a hard and variable spectral component in the 0.3–10 keV range (Walton et al. 2018; Gúrpide et al. 2021). We do not detect pulsations in any individual *XMM−Newton* observation, with only one relatively stringent limit of $\lesssim$20 per cent at frequencies >1 Hz. Even then, we note that pulsations are a transient phenomenon in PULXs and are not seen in all epochs, and indeed the pulsed fraction itself varies in the 0.3–10 keV band, with it dropping below the best limit seen for 4XMM J112054.3+531040 in several observations of NGC 7793 P13 (Fürst et al. 2021) or never exceeding 10 per cent in the faintest of the detected pulsations from NGC 1313 X-2 (Sathyaprakash et al. 2019). It is therefore still eminently possible that further observations of 4XMM J112054.3+531040 could reveal pulsations, and we regard it as a good candidate PULX.

The final object, 4XMM J165251.5−591503, has been shown to likely be a foreground object within our own Galaxy, although its precise nature is not clear. The fact it was not removed from W22 during the composition of that catalogue shows a potential weakness of its selection/rejection criteria – a lack of detailed consideration of Galactic contaminants. Although stars are rejected if spatially coincident with candidate ULXs, this is limited to those in the Tycho 2 catalogue (Høg et al. 2000) and those that are picked up via the Simbad interface (Wenger et al. 2000)[15]. This example shows that more filtering is required to pick up Galactic objects, for example, looking for counterparts with measured parallax at low Galactic latitudes. The 4XMM-DR9 ULX catalogue of Bernadich et al. (2022) performs better than W22 in this regard by searching catalogues

[15] http://simbad.cds.unistra.fr/simbad/

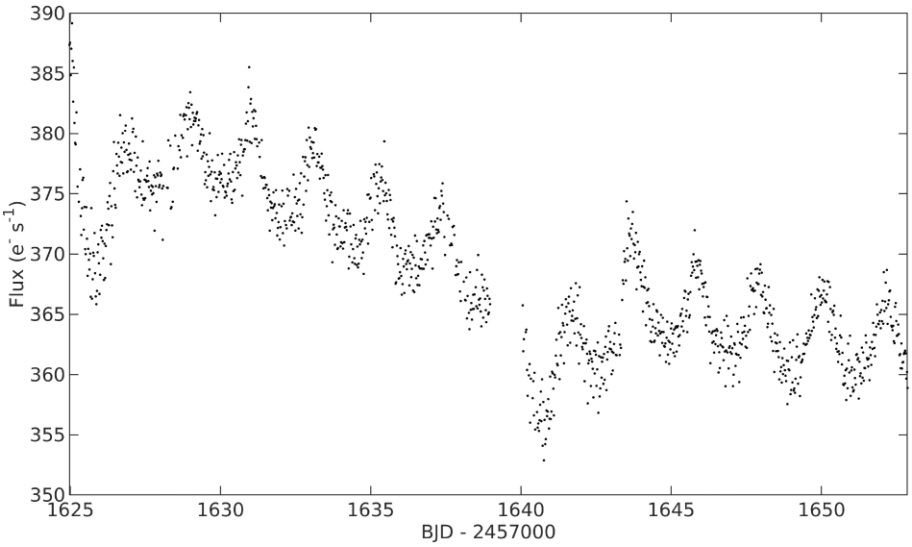

Figure 8. Light curve of the candidate counterpart to 4XMM J165251.5−591503 obtained with 30 min cadence during Sector 12 of the *TESS* mission.

including *Gaia* DR2 for optical point source counterparts to its ULX candidates, and then using the X-ray/optical flux ratios to exclude stars and other objects. The even more recent catalogue of Tranin, Webb & Godet (2023) uses an automated probabilistic classification of X-ray sources to produce a catalogue with a claimed contamination of only 2 per cent. Such stratagems will help to improve future generations of ULX catalogues.

5.2 Are there alternative targets for study from *Chandra* or *Swift*?

In total, our selection strategy revealed three previously unstudied eULXs from a sample of 15 in W22 that had relatively high flux and high luminosity detections in *XMM–Newton* data. The focus on *XMM–Newton* was specifically so that we could select pre-existing data where pulsation searches were possible at frequencies similar to those of the pulsations of known PULXs, which is currently only possible below 10 keV using pn data. It is interesting to ask whether the other mission catalogues analysed in W22 revealed broadly similar eULX candidates; although they might not have *XMM–Newton* data suitable for sensitive pulsation analysis currently available, they would potentially be excellent targets for future observations. We therefore repeated the selection of eULX candidates using the same two simple flux and luminosity criteria but using the ULX catalogues in W22 derived from *Swift* (2SXPS) and *Chandra* (CSC2.0).

The results are shown in Fig. 9. To create this figure, we needed to correct the CSC2.0 data for its narrower (0.5–7 keV) bandpass. For a variety of spectral shapes representative of most ULXs (power-law continua in the range $\Gamma \sim 1.5$–2.5 and absorption column ~ 1–3×10^{21} cm^{-2}), the correction factor is generally in the range 1.1–1.3; we used the optimistic upper value of 1.3 to correct the *Chandra* fluxes and luminosities for each detection of each ULX in the left-hand panel. In the right-hand panel, we show the *Swift* data and have chosen to display the peak flux/luminosity combination for each source (observation-level data is not present for 2SXPS sources in W22, although it is easily recoverable from 2SXPS itself). Clearly, the number of sources chosen from each detector to inhabit the demarcated parameter space varies greatly. There are only seven CSC2.0 detections within the selection region (including one very marginal case, even after the generous correction factor). The five brightest (in flux) are all already in our *XMM–Newton* selection – three separate detections of 4XMM J095550.4+694045 (M82 X-1), and one each of 4XMM J022727.5+333443 (NGC 925 X-1) and 4XMM J131519.5+420301 (NGC 5055 X-1). The two fainter sources are not in the current list, and so present new targets. The 2SXPS data, on the other hand, presents far more potential targets than the *XMM–Newton* selection – a total of 75 eULX candidates with peak flux and luminosity in the correct region of parameter space. Ten of these were in the *XMM–Newton* selection presented in Section 2; those missing include two of the sources presented in this paper (4XMM J091948.8−121429 and 4XMM J165251.5−591503, respectively), M82 X-1, which will have been excluded by W22 for being too close to the nucleus of M82 for *Swift* to resolve it from any putative nuclear activity, 4XMM J151558.6+561810 (NGC 5907 ULX1) whose luminosity peaked in the HLX regime during *Swift* observations, and 4XMM J230457.6+122028 (NGC 7479 ULX-1) where the flux was marginally below the cut-off. Note, however, that if we had chosen instead to use the average *Swift* flux and luminosity per source, we would have obtained a similar outcome to the original *XMM–Newton* selection – 15 sources (albeit the overlap with the *XMM–Newton* selection was only seven objects, with the other eight all new potential targets). The analysis of the data from these new eULX candidates is left to future work.

The lack of *Chandra* sources is puzzling, but may be due to a combination of several factors. These include the narrower bandpass (although an attempt was made to correct for this in the figure); the smaller point spread function, which will be much better at removing contaminants (local diffuse emission and/or other point sources) than is possible for *XMM–Newton* or *Swift*; and perhaps most importantly, the removal of sources from W22 that are quality flagged, which will have removed objects at relatively high fluxes due to the presence of read-out streaks and/or pile-up. The much larger potential target list revealed by *Swift* is likely a consequence of two factors. First, *Swift* has covered a larger sky area than either other mission (e.g. $\sim$3800 deg^2 in 2SXPS, Evans et al. 2020, compared to $\sim$1200 deg^2 in 4XMM-DR10, which is marginally larger than the area covered by 4XMM-DR9 reported in Webb et al. 2020), and so has better coverage of galaxies at moderate distances (<30 Mpc) for which the detection of eULX candidates is possible, even for short *Swift* snapshots. Second, it takes many more observations of individual

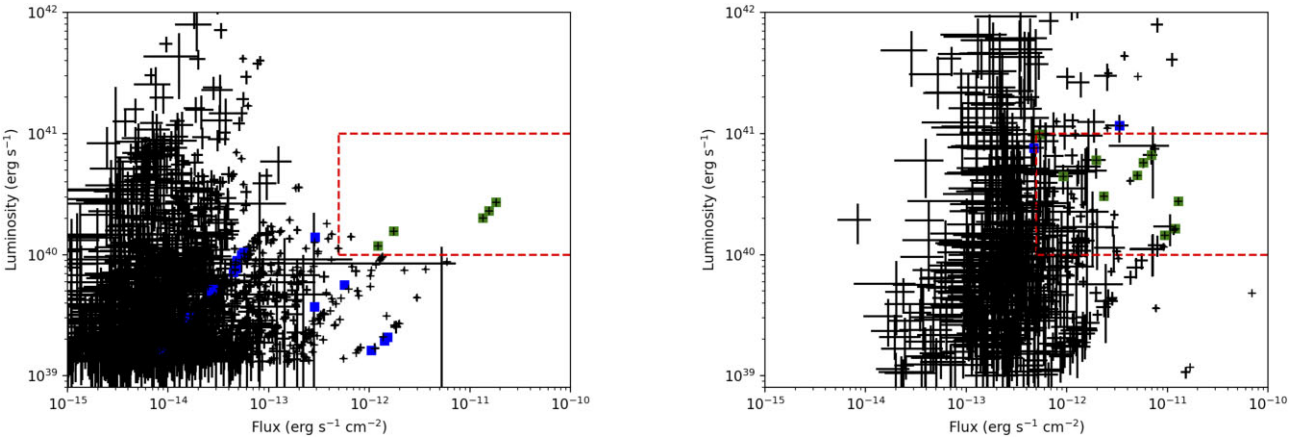

Figure 9. Recreation of Fig. 1, but instead for the CSC2.0 (*left*) and 2SXPS (*right*) ULX candidates from W22. Any of the 15 sources detected by *XMM–Newton* within the region of interest (delineated by the red, dotted line) also detected in the same region of parameter space by *Chandra* or *Swift* are highlighted by a green square. Any of these objects detected but not in the region of interest are highlighted instead by blue squares. The CSC2.0 fluxes and luminosities are all increased by a factor 1.3 to account for its smaller bandpass; the 2SXPS data panel uses the peak values for each individual source (i.e. the highest flux/luminosity combination) from any individual *Swift* observation.

sources, on average, than the other missions. Hence, for ULXs, which are generally a variable population, there are more chances to catch a source in the correct luminosity range. The combination of these two factors bodes well for the detection of eULXs by the *eROSITA* all-sky survey, which will combine multiple visits to the position of each ULX candidate with full sky coverage and sensitivity per visit similar to the *Swift* snapshots.

5.3 Is this a good method for finding PULX candidates?

The starting point for this work was to search for new PULX candidates, using a combination of high flux, high luminosity, and existing *XMM–Newton* data as the selection criteria. This has revealed one new interesting PULX candidate and another object requiring further observations. There are many other potential candidates for observation, as revealed by *Swift* and a couple more by *Chandra*. However, a basic question remains – is this a good way of finding good candidates to be PULXs? This is important to answer, as it helps us to make the best use of limited observational time on X-ray facilities.

There are a couple of alternative approaches that can be taken. Earnshaw et al. (2018) suggested, looking for ULXs that display large amplitude variability, based on the suggestion of Tsygankov et al. (2016), that high amplitude flux variability in M82 X-2 was due to the propeller effect (although it is now unclear whether this is the case or if it is instead variable due to a ∼60 d superorbital period, cf. Brightman et al. 2019). Song et al. (2020) improved upon the Earnshaw work, identifying 17 good candidates including two known PULXs; however, none of the new objects in that sample have yet been identified as PULXs, and the premise of looking for large amplitude variability as evidence for the propeller effect has recently been questioned by Middleton, Gúrpide & Walton (2023) who argue this should instead lead to increased variability in the hard spectral component of ULXs. This is consistent with Walton et al. (2018), who show that known PULXs have a dominant hard spectral component when pulsating, which reduces in strength when they are not doing so.

Indeed, a second method for looking for PULXs is to compare the spectral and timing behaviour of other ULXs to the known PULXs; Gúrpide et al. (2021) suggest good PULX candidates on this basis, but again, no pulsations have been found from these objects yet. However, propeller-induced variability may not be the only reason to continue to look for high amplitude variability in ULXs; Khan et al. (2022) show that if NS-ULXs have a higher degree of geometric beaming than BH-ULXs, then precession of the accretion discs will result in a higher fraction of variable NS-ULXs than BH-ULXs. Therefore, high amplitude variability may remain as a possible marker for PULX candidates even without propeller effects.

In the absence of of any positive results, it is not clear whether any of these suggested strategies provide a better chance of finding detectable PULXs than the others. It is therefore prudent to continue to attempt them all if we wish to maximize our chances of discovering more PULXs, and thereby learn more about the physics of super-Eddington accretion in the regime of high magnetic field compact objects.

6 CONCLUSIONS

We started by posing a question – can we use the fact that most of the small number of PULXs detected to date have observed luminosities that peak in excess 10^{40} erg s^{-1} (i.e. in the eULX regime) to find more PULX candidates? To answer this, we filtered the ULX catalogue of Walton et al. (2022) to select objects with *XMM–Newton* data showing peak luminosities in this range, concurrent with fluxes above 5×10^{-13} erg cm^{-2} s^{-1} (with the latter used to select objects, where we have a good chance of accumulating $>10^4$ counts in an orbit, sufficient to detect pulsations). Most of the 15 objects selected are well-studied ULXs; however, we uncovered three ULXs that have hitherto been largely neglected for study. The analysis of available archival data for these objects is the subject of this paper.

We found 4XMM J165251.5−591503 to be a soft and variable X-ray source. It lies at low Galactic latitude and is coincident with a bright optical/IR source with measured parallax and ∼2 day periodic variability, indicating it is very likely a foreground contaminant. However, a full diagnosis of the nature of this object requires more observations. The presence of a Galactic contaminant highlights a weakness in the filtering of W22 for such objects. However, this could readily be corrected by the use of *Gaia* data and/or the use of statistical/multiwavelength identification techniques to

better identify foreground objects in future catalogues, as has already been done in the work of Bernadich et al. (2022) and Tranin et al. (2023). 4XMM J091948.8−121429 on the other hand remains an excellent eULX candidate but suffers from minimal archival data being available at present, so also requires further observational study to improve our understanding of it. The final object, 4XMM J112054.3+531040 has by far the best current archival data. It shows moderate X-ray variability on time-scales of minutes to years, an X-ray spectrum that is hard and can be modelled similarly to other ULXs, and a local environment in the spiral arm of its host galaxy that appears similar to other ULX environments (including potential counterparts, which indicate an X-ray-to-optical flux ratio that is too high for a background AGN). We are able to perform accelerated pulsation searches on the *XMM–Newton* pn data for this object, but we do not find any pulsations, with the best limits of a pulse fraction $\lesssim$20 per cent for a pulsation at $\sim$1 Hz. So, 4XMM J112054.3+531040 is not at this time a confirmed PULX; it does, however, remain a plausible candidate given its hard X-ray spectrum, moderate limits on the pulsed fraction, and the fact that pulsations are transient characteristics of PULXs. Again, further observations with the current fleet of X-ray observatories are required to better understand the nature of this object.

Finally, we note that the selection of high luminosity, high flux ULXs provides an interesting sample of objects that could be the subject of further study with many future X-ray missions, both imminent and proposed (e.g. *XRISM*, *HEX-P*, *New Athena*, etc.), that could provide new opportunities to investigate whether they host PULXs. We look forward to the excellent science they will enable.

ACKNOWLEDGEMENTS

We thank the anonymous referee for their constructive comments that have helped improve this paper. TPR & SS were supported by the Science and Technology Facilities Council (STFC) as part of consolidated grant ST/T000244/1. ADAM thanks STFC for their support via an STFC studentship (ST/T506047/1). This research has made use of data obtained with *XMM–Newton*, an ESA science mission with instruments and contributions directly funded by ESA Member States and NASA. It has made use of data obtained from the *Chandra* Data Archive and the *Chandra* Source Catalogue, and software provided by the *Chandra* X-ray Center (CXC) in the application package CIAO. This work made use of data supplied by the UK *Swift* Science Data Centre at the University of Leicester. It uses observations made with the NASA/ESA *Hubble Space Telescope*, and obtained from the Hubble Legacy Archive, which is a collaboration between the Space Telescope Science Institute (STScI/NASA), the Space Telescope European Coordinating Facility (ST-ECF/ESAC/ESA), and the Canadian Astronomy Data Centre (CADC/NRC/CSA). This paper includes data collected with the *TESS* mission, obtained from the MAST data archive at the STScI. Funding for the *TESS* mission is provided by the NASA Explorer Program. STScI is operated by the Association of Universities for Research in Astronomy, Inc., under NASA contract NAS 5Ð26555. The Pan-STARRS1 Surveys (PS1) and the PS1 public science archive have been made possible through contributions by the Institute for Astronomy, the University of Hawaii, the Pan-STARRS Project Office, the Max-Planck Society, and its participating institutes, the Max Planck Institute for Astronomy, Heidelberg, and the Max Planck Institute for Extraterrestrial Physics, Garching, The Johns Hopkins University, Durham University, the University of Edinburgh, the Queen's University Belfast, the Harvard-Smithsonian Center for Astrophysics, the Las Cumbres Observatory Global Telescope Network Incorporated, the National Central University of Taiwan, the Space Telescope Science Institute, the National Aeronautics and Space Administration under Grant No. NNX08AR22G issued through the Planetary Science Division of the NASA Science Mission Directorate, the National Science Foundation Grant No. AST-1238877, the University of Maryland, Eotvos Lorand University (ELTE), the Los Alamos National Laboratory, and the Gordon and Betty Moore Foundation. This work has made use of data from the European Space Agency (ESA) mission *Gaia* (https://www.cosmos.esa.int/gaia), processed by the *Gaia* Data Processing and Analysis Consortium (DPAC, https://www.cosmos.esa.int/web/gaia/dpac/consortium). Funding for the DPAC has been provided by national institutions, in particular the institutions participating in the *Gaia* Multilateral Agreement. This research has made use of the NASA/IPAC Extragalactic Database (NED), which is operated by the Jet Propulsion Laboratory, California Institute of Technology, under contract with the National Aeronautics and Space Administration. It has also made use of NASA's Astrophysics Data System.

DATA AVAILABILITY

The data used in this paper is all available from public archives, via searches for the observation identifiers in Table 2 and/or the text, or via searches at the positions of the three sources studied. *XMM–Newton* data was obtained from the *XMM–Newton* Science Archive (XSA) (https://www.cosmos.esa.int/web/xmm-newton/xsa) and *Chandra* data was obtained from the *Chandra* Data Archive (https://cxc.cfa.harvard.edu/cda/). The *Swift* data was all obtained from 2SXPS (https://www.swift.ac.uk/2SXPS/). Pan-STARRS imaging data was obtained from http://ps1images.stsci.edu/cgi-bin/ps1cutouts, and *HST* data was obtained from MAST (https://archive.stsci.edu). The TESS data used in the analysis of this work is available on the MAST webpage (https://mast.stsci.edu/portal/Mashup/Clients/Mast/Portal.html). *Gaia* data was obtained via the VizieR interface for astronomical catalogues (https://vizier.cds.unistra.fr).

REFERENCES

Aird J. et al., 2010, MNRAS, 401, 2531
Arbour R., 2016, TNS Discovery Report, 2016, 1
Bachetti M. et al., 2013, ApJ, 778, 163
Bachetti M. et al., 2014, Nature, 514, 202
Bachetti M. et al., 2022, StingraySoftware/stingray: Version 1.0, https://doi.org/10.5281/zenodo.6394742
Bañados E. et al., 2018, Nature, 553, 473
Berghea C. T., Weaver K. A., Colbert E. J. M., Roberts T. P., 2008, ApJ, 687, 471
Bernadich M. C. i., Schwope A. D., Kovlakas K., Zezas A., Traulsen I., 2022, A&A, 659, A188
Brightman M. et al., 2019, ApJ, 873, 115
Brightman M., Walton D. J., Xu Y., Earnshaw H. P., Harrison F. A., Stern D., Barret D., 2020, ApJ, 889, 71
Colbert E. J. M., Mushotzky R. F., 1999, ApJ, 519, 89
Colbert E. J. M., Ptak A. F., 2002, ApJS, 143, 25
Cutri R. M. et al., 2003, 2MASS All Sky Catalog of point sources
Dall'Osso S., Perna R., Stella L., 2015, MNRAS, 449, 2144
Dickey J. M., Lockman F. J., 1990, ARA&A, 28, 215
Earley N. M., Dwarkadas V. V., Cirillo V., 2021, Universe, 8, 18
Earnshaw H. P., Roberts T. P., Sathyaprakash R., 2018, MNRAS, 476, 4272
Evans P. A. et al., 2020, ApJS, 247, 54
Fabbiano G., Trinchieri G., 1987, ApJ, 315, 46
Farrell S. A., Webb N. A., Barret D., Godet O., Rodrigues J. M., 2009, Nature, 460, 73

Feng H., Kaaret P., 2006, ApJ, 650, L75
Fürst F. et al., 2016, ApJ, 831, L14
Fürst F. et al., 2021, A&A, 651, A75
Fürst F. et al., 2023, A&A, 672, A140
Fürst F., Walton D. J., Stern D., Bachetti M., Barret D., Brightman M., Harrison F. A., Rana V., 2017, ApJ, 834, 77
Gaia Collaboration, 2022, A&A, 674, A1
Gladstone J. C., 2013, Mem. Soc. Astron. Italiana, 84, 629
Gladstone J. C., Roberts T. P., Done C., 2009, MNRAS, 397, 1836
Granata V. et al., 2016, Astron. Telegram, 8818, 1
Guainazzi M., Rodriguez-Pascual P., Fabian A. C., Iwasawa K., Matt G., 2004, MNRAS, 355, 297
Güdel M., 2004, A&A Rev., 12, 71
Gúrpide A., Godet O., Koliopanos F., Webb N., Olive J. F., 2021, A&A, 649, A104
Heil L. M., Vaughan S., Roberts T. P., 2009, MNRAS, 397, 1061
Hodges-Kluck E. J., Bregman J. N., Miller J. M., Pellegrini E., 2012, ApJ, 747, L39
Høg E. et al., 2000, A&A, 355, L27
Huppenkothen D. et al., 2019, ApJ, 881, 39
Iłkiewicz K. et al., 2021, MNRAS, 503, 4050
Israel G. L. et al., 2017a, Science, 355, 817
Israel G. L. et al., 2017b, MNRAS, 466, L48
Kaaret P., Feng H., 2013, ApJ, 770, 20
Kaaret P., Feng H., Roberts T. P., 2017, ARA&A, 55, 303
Kaaret P., Simet M. G., Lang C. C., 2006, ApJ, 646, 174
Khan N., Middleton M. J., Wiktorowicz G., Dauser T., Roberts T. P., Wilms J., 2022, MNRAS, 509, 2493
King A. R., Davies M. B., Ward M. J., Fabbiano G., Elvis M., 2001, ApJ, 552, L109
Kluzniak W., Lasota J. P., 2015, MNRAS, 448, L43
Koliopanos F., Vasilopoulos G., Godet O., Bachetti M., Webb N. A., Barret D., 2017, A&A, 608, A47
Kosec P. et al., 2021, MNRAS, 508, 3569
Kovlakas K., Zezas A., Andrews J. J., Basu-Zych A., Fragos T., Hornschemeier A., Lehmer B., Ptak A., 2020, MNRAS, 498, 4790
Krivonos R., Sazonov S., 2016, MNRAS, 463, 756
Liu J., 2011, ApJS, 192, 10
Mak D. S. Y., Pun C. S. J., Kong A. K. H., 2011, ApJ, 728, 10
Matsumoto H., Tsuru T. G., Koyama K., Awaki H., Canizares C. R., Kawai N., Matsushita S., Kawabe R., 2001, ApJ, 547, L25
Mezcua M., Roberts T. P., Lobanov A. P., Sutton A. D., 2015, MNRAS, 448, 1893
Middleton M. J., King A., 2017, MNRAS, 470, L69
Middleton M., Gúrpide A., Walton D. J., 2023, MNRAS, 519, 2224
Mineo S., Gilfanov M., Sunyaev R., 2012, MNRAS, 419, 2095
Mondal S., Belczyński K., Wiktorowicz G., Lasota J.-P., King A. R., 2020a, MNRAS, 491, 2747
Mondal S., Różańska A., Lai E. V., De Marco B., 2020b, A&A, 642, A94
Motch C., Pakull M. W., Soria R., Grisé F., Pietrzyński G., 2014, Nature, 514, 198
Mushtukov A. A., Ingram A., Middleton M., Nagirner D. I., van der Klis M., 2019, MNRAS, 484, 687
Mushtukov A. A., Suleimanov V. F., Tsygankov S. S., Poutanen J., 2015, MNRAS, 454, 2539
Pakull M. W., Mirioni L., 2002, preprint (astro–ph/0202488)
Pasham D. R., Strohmayer T. E., Mushotzky R. F., 2014, Nature, 513, 74
Pinto C. et al., 2020, MNRAS, 492, 4646
Pinto C., Middleton M. J., Fabian A. C., 2016, Nature, 533, 64
Pintore F. et al., 2018, MNRAS, 479, 4271
Pintore F., Zampieri L., Stella L., Wolter A., Mereghetti S., Israel G. L., 2017, ApJ, 836, 113
Pintore F., Zampieri L., Sutton A. D., Roberts T. P., Middleton M. J., Gladstone J. C., 2016, MNRAS, 459, 455
Prestwich A. H., Jackson F., Kaaret P., Brorby M., Roberts T. P., Saar S. H., Yukita M., 2015, ApJ, 812, 166
Pye J. P., Rosen S., Fyfe D., Schröder A. C., 2015, A&A, 581, A28
Rana V. et al., 2015, ApJ, 799, 121
Ransom S. M., Eikenberry S. S., Middleditch J., 2002, AJ, 124, 1788
Read A. M., Pietsch W., 1999, A&A, 341, 8
Roberts T. P., Levan A. J., Goad M. R., 2008, MNRAS, 387, 73
Roberts T. P., Warwick R. S., 2000, MNRAS, 315, 98
Salvaggio C. et al., 2022, MNRAS, 512, 1814
Sathyaprakash R. et al., 2019, MNRAS, 488, L35
Schlafly E. F., Finkbeiner D. P., 2011, ApJ, 737, 103
Song X., Walton D. J., Lansbury G. B., Evans P. A., Fabian A. C., Earnshaw H., Roberts T. P., 2020, MNRAS, 491, 1260
Sridhar N., Metzger B. D., Beniamini P., Margalit B., Renzo M., Sironi L., Kovlakas K., 2021, ApJ, 917, 13
Stobbart A. M., Roberts T. P., Wilms J., 2006, MNRAS, 368, 397
Strickland D. K., Colbert E. J. M., Heckman T. M., Weaver K. A., Dahlem M., Stevens I. R., 2001, ApJ, 560, 707
Sutton A. D., Roberts T. P., Gladstone J. C., Farrell S. A., Reilly E., Goad M. R., Gehrels N., 2013a, MNRAS, 434, 1702
Sutton A. D., Roberts T. P., Middleton M. J., 2013b, MNRAS, 435, 1758
Sutton A. D., Roberts T. P., Walton D. J., Gladstone J. C., Scott A. E., 2012, MNRAS, 423, 1154
Swartz D. A., Soria R., Tennant A. F., Yukita M., 2011, ApJ, 741, 49
Tranin H., Webb N., Godet O., 2023, preprint (arXiv:2304.11216)
Tsygankov S. S., Mushtukov A. A., Suleimanov V. F., Poutanen J., 2016, MNRAS, 457, 1101
Vaughan S., Edelson R., Warwick R. S., Uttley P., 2003, MNRAS, 345, 1271
Walton D. J. et al., 2016, ApJ, 827, L13
Walton D. J. et al., 2018, ApJ, 856, 128
Walton D. J., Mackenzie A. D. A., Gully H., Patel N. R., Roberts T. P., Earnshaw H. P., Mateos S., 2022, MNRAS, 509, 1587
Walton D. J., Roberts T. P., Mateos S., Heard V., 2011, MNRAS, 416, 1844
Wang S., Liu J., Qiu Y., Bai Y., Yang H., Guo J., Zhang P., 2016, ApJS, 224, 40
Webb N. A. et al., 2020, A&A, 641, A136
Wenger M., et al., 2000, A&AS, 143, 9
Whitmore B.C. et al., 2016, AJ, 151, 134
Wilms J., Allen A., McCray R., 2000, ApJ, 542, 914

This paper has been typeset from a TEX/LATEX file prepared by the author.